Inorganic Chemistry

pubs.acs.org/IC

Article

Investigation of the $Cs_2(Mo,Te)O_4$ Solid Solution and Implications on the Joint Oxyde-Gaine System in Fast Neutron Reactors

Enrica Epifano, Andrea Volfi, Maas Abbink, Hendrik Nieuwland, Lambert van Eijck, Gilles Wallez, Dipanjan Banerjee, Philippe M. Martin, and Anna L. Smith*

Cite This: *Inorg. Chem.* 2020, 59, 10172−10184

Read Online

ACCESS | Metrics & More | Article Recommendations | Supporting Information

ABSTRACT: The formation of a thin layer, the so-called Joint Oxyde-Gaine (JOG), between the $(U,Pu)O_2$ fuel pellets and the cladding has been observed in fast neutron reactors, due to the accumulation of volatile fission products. Cs_2MoO_4 is known to be one of the major components of the JOG, but other elements are also present, in particular tellurium and palladium. In this work, an investigation of the structural and thermodynamic properties of Cs_2TeO_4 and $Cs_2Mo_{1-x}Te_xO_4$ solid solution is reported. The existence of a complete solubility between Cs_2MoO_4 and Cs_2TeO_4 is demonstrated, combining X-ray diffraction (XRD), neutron diffraction (ND), and X-ray absorption spectroscopy (XAS) results. High-temperature XRD measurements were moreover performed on Cs_2TeO_4, which revealed the existence of a $\alpha-\beta$ phase transition around 712 K. Thermal expansion coefficients were also obtained from these data. Finally, phase equilibra points in the $Cs_2MoO_4-Cs_2TeO_4$ pseudobinary phase diagram were collected using differential scanning calorimetry and used to develop a thermodynamic model for this system using a regular solution formalism.

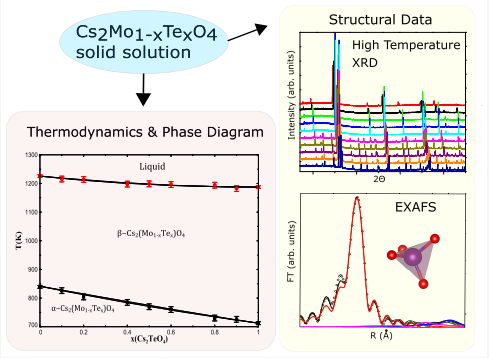

1. INTRODUCTION

The Generation IV International Forum is currently investigating innovative nuclear reactor designs which should lead to improved safety, sustainability, and efficiency.[1] Among the considered designs, fast neutron reactors (FNRs), such as the sodium-cooled and lead-cooled reactors, are very promising as they would allow achieving higher thermal efficiencies than currently used Light-Water Reactors (LWRs), by operating at higher temperatures. Mixed uranium−plutonium oxide (or MOX) pellets, enclosed inside a stainless steel cladding, are currently the preferred choice for the fuel in these reactors. The behavior of these materials in FNR conditions is currently under investigation. Various irradiation tests and post-irradiation examinations of MOX fuels in FNR prototypes have shown a specific behavior not previously observed in the light-water reactor fuels. In particular, the formation of an oxide fission products layer (up to a few hundred micrometers in thickness) between the fuel and the cladding, named "Joint Oxyde-Gaine" or JOG (the French term for the oxide-cladding joint), has been observed.[2−8] This layer is formed by volatile and semi-volatile fission product elements, mainly cesium, molybdenum, iodine, tellurium, and palladium, that migrate from the center of the fuel pellet ($T \simeq$ 2300 K) toward the edge, due to the strong radial thermal gradient ($\simeq$450 K mm^{-1}), and accumulate between the fuel and the cladding, where the temperature is lower ($T \simeq$ 973 K). Knowing the thermal and mechanical properties of this layer is crucial for the safety assessment of the reactor. The irradiated fuel-cladding interaction needs to be well understood and controlled to prevent the release of radioactive elements from the fuel into the main circuit. The formation of the JOG layer could induce mechanical stresses on the cladding or drops in thermal conductivity, leading to creation of hot spots and local melting, and to an acceleration of the cladding corrosion. All these effects could cause a failure of the cladding integrity, and for this reason, the JOG needs to be investigated and accounted for in Fuel Performance Codes.

The JOG is a complex, multi-element system, including Cs−Mo−Te−Pd−Ba−I−U−O chemical elements stable in the forms of Cs_2MoO_4, CsI, Cs_2Te, etc.[9] The main crystalline phase in the JOG is Cs_2MoO_4, according to post-irradiation examinations (PIE)[8] and thermochemical calculations.[9−11] The thermodynamic properties of this phase and the phase equilibria in the Cs−Mo−O system are relatively well known.[12−14] However, a thorough knowledge of the JOG thermodynamic behavior requires also the investigation of the other subsystems, for which data are still missing, as for

Received: May 2, 2020
Published: June 25, 2020

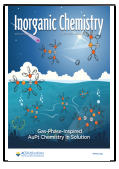

https://dx.doi.org/10.1021/acs.inorgchem.0c01307
Inorg. Chem. 2020, 59, 10172−10184

instance the Cs−Te−O system, which presents several ternary compounds. Loopstra and Goubitz identified the crystallographic structures of three cesium tellurites, namely, Cs_2TeO_3, $Cs_2Te_2O_5$, and $Cs_2Te_4O_9$, as well as a mixed valence state compound of chemical formula $Cs_2Te_4O_{12}$.[15,16] The crystallographic structure of the cesium tellurate, Cs_2TeO_4, was identified by Weller et al.[17] The only available phase diagram data refer to a differential scanning calorimetry (DSC) study of the TeO_2−Cs_2TeO_3 pseudo-binary system,[18] while the available thermodynamic data are limited to the enthalpies of formation of Cs_2TeO_3, $Cs_2Te_2O_5$, $Cs_2Te_4O_9$, and Cs_2TeO_4.[19] Further studies are hence necessary in order to completely determine the Cs−Te−O phase equilibria and the possible effects on the JOG system.

This work focuses on the Cs_2TeO_4 compound and the $Cs_2(Mo,Te)O_4$ solid solution. The Cs_2TeO_4 phase is of particular interest for the JOG as it is iso-structural with Cs_2MoO_4. The existence of a complete $Cs_2(Mo,Te)O_4$ solid solution is shown herein. The structural properties of Cs_2TeO_4 and mixed compounds are investigated by combining X-ray diffraction (XRD), neutron diffraction (ND), and X-ray absorption spectroscopy (XAS) measurements. The polymorphism of Cs_2TeO_4 is investigated using high-temperature (HT) XRD, and the coefficients of thermal expansion are assessed from the measured data. Differential scanning calorimetry (DSC) is used to investigate phase equilibria in the Cs_2MoO_4−Cs_2TeO_4 system, in particular to determine phase transition temperatures and associated enthalpies. Finally, a thermodynamic model of the Cs_2MoO_4−Cs_2TeO_4 system is reported using a regular solution formalism, based on the collected experimental data.

2. EXPERIMENTAL METHODS

2.1. Sample Preparation. $Cs_2Mo_{1-x}Te_xO_4$ samples were synthesized by reaction between Cs_2MoO_4 and Cs_2TeO_4 powders. Stoichiometric mixtures with x = Te/(Te + Mo) = 5, 10, 20, 40, 50, 60, 80, and 90 at. % were placed in alumina boats and heated under oxygen flow at 873 K, for a total duration of ∼50 h. One intermediate regrinding step has been performed, inside an argon-filled glovebox, to ensure a complete reaction between the two end-members. The Cs_2MoO_4 precursor was prepared starting from Cs_2CO_3 (Alpha Aesar, 99.99%) and MoO_3 (Alpha Aesar, 99.95%), according to the procedure described in ref 20. The obtained powder was white/light yellow. The Cs_2TeO_4 precursor was prepared by solid-state reaction between Cs_2CO_3 and TeO_2 (Alpha Aesar, 99.99%) at 873 K in oxygen flow (O_2, ≥99.5%, rest Ar and N_2, H_2O < 1500 vpm) for ∼60 h. The powder exhibited a light gray color. Immediately after the synthesis, the samples were transferred in an argon-filled glovebox, with dry atmosphere, where the H_2O and O_2 contents were kept below 5 ppm. The handling of the samples was always done inside this glovebox, because of the hygroscopic nature of the synthesized materials.

2.2. X-ray Powder Diffraction (XRD). Room-temperature X-ray diffraction measurements were carried out using a PANalytical X'Pert PRO X-ray diffractometer mounted in the Bragg−Brentano configuration with a Cu anode (0.4 mm × 12 mm line focus, 45 kV, 40 mA). The X-ray scattered intensities were measured with a real-time multi-strip (RTMS) detector (X'Celerator). The powdered samples were placed in a sealed sample holder, with a kapton foil cover, to maintain the dry argon atmosphere during the XRD measurement. The data were collected by step scanning in the angle range $10° \leq 2\theta \leq 120°$, with a step size of 0.008° (2θ); one single scan was performed, for a total measuring time of about 8 h. Structural analysis was performed by the Rietveld method with the FullProf Suite.[21] The displacement of the sample surface with respect to the goniometer was refined and compared to that of a gold powder standard, which was measured using the same sample holder. In all the cases, comparable displacements were obtained from the refinement.

2.3. High-temperature X-ray Powder Diffraction (HT-XRD). High-temperature XRD experiments were carried out from 298 to 1073 K in Bragg−Brentano mode on a Panalytical X'Pert Pro diffractometer equipped with an Anton Parr furnace, using the Cu−Kα_1 radiation (Ge (111) monochromator). Measurements were performed under a silica gel-dried air flow. Each pattern was recorded by scanning the 16−80° 2θ range, with a step size of 0.013°, and using a 1 h 40 min counting time. The data were treated by Rietveld analysis using the FullProf Suite[21] in order to refine the lattice and structure parameters. Irregular peak shapes were observed and attention was paid to their origin. Lattice distortions were considered, but finally ruled out, and the irregular peak shapes were attributed to the small amount of powder, which only covered part of the holder's surface. These imperfections were eventually corrected by introducing a secondary "fictional" phase in the refinement, and a geometric intensity correction for incomplete illumination was applied. The two phases (in a 95:5 ratio according to the refinements) were given the same set of atomic coordinates but independent cell edges. As the thermal evolution was found to be similar for the two phases, the computation of the thermal expansion was made on the parameters of the main one.

Due to strong differences in electron densities between oxygen and the heavy Cs and Te cations, soft constraints were applied to the Te−O bond lengths. Likewise, a single B_0 (isotropic atomic displacement) value was used for all the oxygen atoms, whereas independent anisotropic factors were refined for the cations.

2.4. Neutron Diffraction (ND). Neutron diffraction (ND) data were recorded at the PEARL beamline at the Hoger Onderwijs Reactor at TU Delft.[22] The sample was encapsulated in a cylindrical, vanadium can (50 mm high, 6 mm inner diameter) closed with a Viton O-ring. This preparation step was performed inside the glovebox, under dry argon atmosphere. The data were collected at room temperature, at a fixed wavelength (λ = 1.667 Å) over the range $11° < 2\theta < 158°$. The "instrumental background" (including the contribution from the sample can) was subtracted from the recorded data. Structural analysis was performed by the Rietveld method with the FullProf Suite.[21]

2.5. X-ray Absorption Spectroscopy (XAS). X-ray absorption spectroscopy (XAS) measurements were performed at the BM26A-DUBBLE beamline[23] of the European Synchrotron Radiation Facility (ESRF) in Grenoble, France. Samples for XAS measurements were prepared inside an argon-filled glovebox. Powdered samples were mixed with boron nitride, pressed in pellets of 5 mm diameter, and encapsulated in kapton foil. The mass of the investigated compounds, ranging from 15 to 50 mg, was optimized in order to correspond to 1−2 absorption lengths. The storage ring operating conditions at the ESRF were 6.0 GeV and 170−200 mA. A Si(111) crystal monochromator was used to select the energy, and calibration was performed using metallic molybdenum (E_{K-edge} = 20000 eV) and tin (E_{K-edge} = 29200 eV) as standard materials for the Mo and Te (E_{K-edge} = 31814 eV) K-edges, respectively.

The XAS data were collected at room temperature in transmission mode. XANES spectra were recorded at first, with a step size of 1 eV and a counting time of 3 s per step. This corresponds to an acquisition time of about 20 min per spectrum. For each compound/edge, at least four scans were collected and at least two different spots of the samples were probed. No modifications were observed among these scans. This indicates that changes of the chemical state due to the beam interaction are unlikely, unless these occurred very quickly, within the first few seconds/minutes of the measurement.

Subsequently, EXAFS spectra were collected at the Mo K-edge, with a counting time increasing with energy, from 3 (XANES part) up to 9 s per step. Between four and ten spectra were acquired for each sample, depending on the quality of the data.

XANES (X-ray absorption near edge structure) spectra were normalized using the ATHENA software,[24] adopting linear functions

https://dx.doi.org/10.1021/acs.inorgchem.0c01307
Inorg. Chem. 2020, 59, 10172−10184

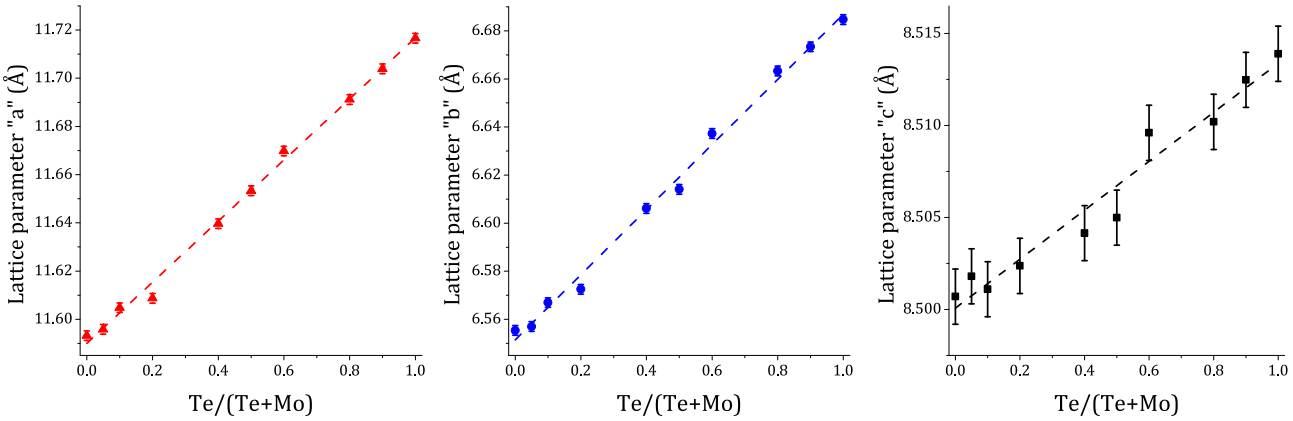

Figure 1. Variation of the lattice parameters as a function of Te/(Te + Mo) content in the $Cs_2Mo_{1-x}Te_xO_4$ solid solution: symbols = experimental points; dashed line = linear fit according to Vegard's law.

for pre-edge and post-edge fitting. The absorption edges were identified as the first zero-crossing of the second derivatives.

EXAFS (extended X-ray absorption fine structure) oscillations were also extracted with the ATHENA software[24] and Fourier-transformed using a Hanning window (3.5−14 $Å^{-1}$, dk = 2 $Å^{-1}$). Interatomic scattering path phases and amplitudes were calculated with the FEFF 8.40 ab initio code.[24] Fitting of the EXAFS data was performed simultaneously in k, k^2, and k^3, using the ARTEMIS software.[24] During the fit, the amplitude prefactor S_0^2 was initially set at 0.95, while the shift in the threshold energy ΔE_0, the interatomic distances, the Debye−Waller factors, and the coordination numbers were optimized. Once the fit reached a sufficient goodness-of-fit, the S_0^2 value was also fitted. The variations from the initial value were negligible. Similar ΔE_0 values were obtained for all the Mo K-edge spectra, between 0.5 and 0.8 eV.

2.6. Differential Scanning Calorimetry (DSC). The phase transition, congruent melting (for Cs_2MoO_4 and Cs_2TeO_4) and solidus temperatures of $Cs_2Mo_{1-x}Te_xO_4$ solid solutions were determined by 3D-heat flux DSC measurements using a Setaram Multi HTC module of the 96 Line calorimeter. The samples were heated inside an alumina crucible under oxygen flow. The temperature was monitored throughout the experiments by a series of interconnected S-type thermocouples. The temperature on the heating ramp (10 K min^{-1}) was calibrated and corrected for the effect of the heating rate by measuring the melting points of standard high purity metals (In, Sn, Pb, Al, Ag, Au) at 2−4−6−8−10−12 K min^{-1}. The calibration procedure was performed as recommended by Höne et al.[25] and Gatta et al.[26] The transition, congruent melting temperature of Cs_2MoO_4 (respectively, Cs_2TeO_4) and solidus temperatures of $Cs_2Mo_{1-x}Te_xO_4$ solid solutions were derived on the heating ramp as the onset temperature using tangential analysis of the recorded heat flow. The uncertainty on the measured temperatures is estimated to be ±5 K for the Cs_2MoO_4 and Cs_2TeO_4 end-members and ±10 K for the transitions of the solid solutions.

The enthalpies of transition between the low-temperature orthorhombic structure and the high-temperature hexagonal structure of $Cs_2Mo_{1-x}Te_xO_4$ solid solutions were moreover determined by placing a reference material of well-known fusion enthalpy (Al and Na_2MoO_4 in this work) in the reference crucible and measuring both sample and reference materials in the same cycle, under argon flow when using the Al reference and under oxygen flow when using the Na_2MoO_4 reference. This configuration allows to calculate for each individual measurement cycle the detector sensitivity equal to

$$s_{ref} = \frac{M_{ref}A_{ref}}{m_{ref}\Delta_{tr}H_m^{\circ}(T_{tr,ref})} \quad (1)$$

where s_{ref} is the detector sensitivity in μV mW^{-1}, M_{ref} the molar mass in g mol^{-1}, m_{ref} the weight of the reference in mg, A_{ref} the peak area corresponding to the transition event in μV s, and $\Delta_{tr}H_m^{\circ}(T_{tr,ref})$ the enthalpy of transition of the reference material in J mol^{-1}.

The detector sensitivity is assumed to remain the same at the temperature of the transition event of the sample, which is a reasonable approximation for two events sufficiently close to each other.

3. RESULTS

3.1. Lattice Parameters Determination of the $Cs_2Mo_{1-x}Te_xO_4$ Solid Solution. Cs_2MoO_4 and Cs_2TeO_4 show, at room temperature, the same orthorhombic structure, with space group *Pcmn*, n.°62 (noted "α" or "o" in this work). The XRD patterns acquired (at room temperature) on the (Cs_2MoO_4:Cs_2TeO_4) mixtures with x = Te/(Te + Mo) = (0.05, 0.10, 0.20, 0.40, 0.50, 0.60, 0.80, and 0.90) exhibited one single phase, indicating the existence of a complete solid solution for the entire composition range. The lattice parameters were obtained by Rietveld refinements of the XRD patterns, and the results are shown in Figure 1, as a function of the Te/(Te + Mo) ratio.

For each lattice parameter (a, b, c), a linear variation is observed, indicating the validity of Vegard's law for this solid solution. The general lattice parameter y of the $Cs_2Mo_{1-x}Te_xO_4$ solid solution, at room temperature, can be expressed as a function of the tellurium content x as

$$y = y_0 + mx \quad (2)$$

The y_0 and m values were obtained by fitting the XRD lattice parameters, and the values are reported in Table 1. The

Table 1. Fitting Parameters Assuming Vegard's Law: $y = y_0 + mx$

	y_0 (Å)	m (Å)	R^2
a (Å)	11.590 ± 0.002	0.127 ± 0.003	0.996
b (Å)	6.552 ± 0.002	0.135 ± 0.004	0.995
c (Å)	8.500 ± 0.001	0.013 ± 0.001	0.960

obtained m values are about ten times larger for the a and b axes than for the c axis, indicating that the substitution of Mo with Te causes an anisotropic expansion of the lattice. The in-deep examination of the α-Cs_2MoO_4 crystal structure by Wallez et al.[20] revealed that the cell edges in the (001) basal plane are ruled by an array of short, strong bonds; on the contrary, the connections between these planes, along the c axis, depend on long, loose Cs−O bonds. This is consistent with what is observed here for the solid solution, i.e., the substitution of Mo^{6+} (ionic radius = 0.41 Å[27]) with Te^{6+} (ionic

https://dx.doi.org/10.1021/acs.inorgchem.0c01307
Inorg. Chem. 2020, 59, 10172−10184

radius = 0.43 Å[27]) results in a marked increase of the parameters in the basal plane (*ab*), whereas the length of the third edge (*c*), which is less dependent on the Mo^{6+} \ Te^{6+}−O bond lengths, undergoes a lesser increase.

3.2. Neutron Diffraction Measurements on Cs_2TeO_4 and $Cs_2Te_{0.5}Mo_{0.5}O_4$. Neutron diffraction data were collected on pure Cs_2TeO_4 and on the $Cs_2Te_{0.5}Mo_{0.5}O_4$ solid solution. As already shown by XRD, both these materials exhibit an orthorhombic structure at room temperature, with the space group *Pcmn*, n°62. The neutron diffraction pattern and the relative fit of Cs_2TeO_4 is shown in Figure 2 (very similar

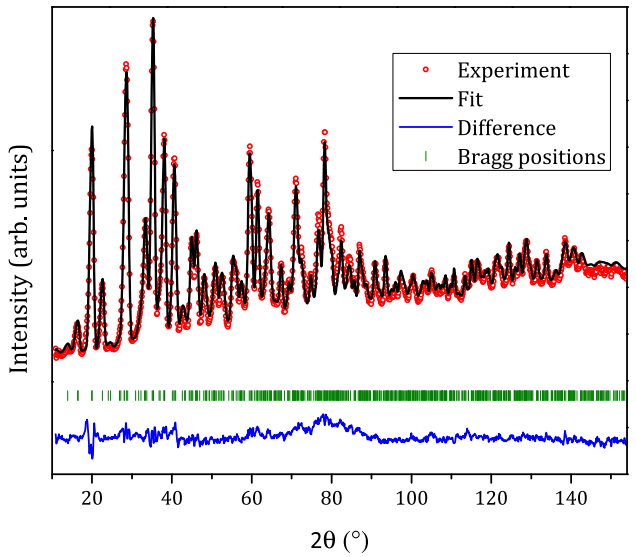

Figure 2. Experimental (red dots) and calculated (black line) neutron diffraction pattern of Cs_2TeO_4. The difference is indicated in blue and the green marks represent the Bragg reflections. Measurement at λ = 1.667 Å. The background was taken as linear interpolation between operator-selected points in the pattern with refinable heights. Goodness-of-fit parameters are R_{wp} = 12.5, R_p = 15.9, χ^2 = 9.51.

results are obtained for $Cs_2Te_{0.5}Mo_{0.5}O_4$, as shown in Figure S1). The refined lattice parameters are *a* = 11.698(2) Å, *b* = 6.675(1) Å, and *c* = 8.502(1) Å, for Cs_2TeO_4 and are *a* = 11.631(2) Å, *b* = 6.607(1) Å, and *c* = 8.494(1) Å, for $Cs_2Te_{0.5}Mo_{0.5}O_4$ (see Table 2). These lattice parameter values

Table 2. Refined Profile Parameters of Cs_2TeO_4 and $Cs_2(Mo_{0.5}Te_{0.5})O_4$ from the ND Data

chemical formula	Cs_2TeO_4	$Cs_2(Mo_{0.5}Te_{0.5})O_4$
crystal system	orthorhombic	
space group (no.)	62, *Pcmn* setting	
Z	4	
source	neutron diffraction (ND)	
wavelength λ (Å)	1.667	1.667
formula weight (g mol^{-1})	425.77	441.59
a (Å)	11.698(2)	11.631(2)
b (Å)	6.675(1)	6.607(1)
c (Å)	8.502(1)	8.494(1)
cell volume *V* (Å^3)	663.9(2)	652.7(2)
d-space range (Å)	0.78−8.35	0.78−8.35
χ^2	9.51	5.33
R_p	15.9	13.4
R_{wp}	12.5	11.6

are consistent with those previously obtained by XRD, even if slightly lower. This difference is not surprising since the lattice parameters obtained from neutron diffraction data are generally less accurate than those from XRD. Moreover, comparing the values to those previously obtained from neutron diffraction on Cs_2MoO_4 (*a* = 11.5623(8) Å, *b* = 6.5406(4) Å, *c* = 8.4906(5) Å[28]), it can be noticed that the lattice parameters of the $Cs_2Te_{0.5}Mo_{0.5}O_4$ solid solution are almost exactly equal to the average values of the two end-members. This confirms again the validity of Vegard's law.

The atomic positions, as obtained from the neutron data refinement, are reported in Table 3. The $Cs_2Mo_{1-x}Te_xO_4$ structure, shown in Figure 3, consists of isolated and slightly distorted TeO_4 (respectively, MoO_4) tetrahedra linked by Cs^+ cations in 9- and 10-fold coordination.

3.3. Valence State Determination by XANES. X-ray absorption near-edge structure (XANES) spectra were collected at the Mo K-edge on pure Cs_2MoO_4 and $Cs_2Mo_{1-x}Te_xO_4$ solid solutions with *x* = 0.05, 0.10, 0.50, and 0.80. The results are shown in Figure 4a and are compared to standard materials, namely, metallic Mo^0, $Mo^{IV}O_2$, and $Mo^{VI}O_3$ oxides. Similarly, XANES data were collected at the Te K-edge for Cs_2TeO_4 and the mixed compounds with *x* = 0.50 and 0.80 (for the lower Te concentration, the absorption at the Te K-edge was too low); these spectra, shown in Figure 4b, are compared to those of $Te^{IV}O_2$ and $Cs_2Te_4{}^{IV}O_9$. We remark here that, to the best of our knowledge, this is the first time that XANES data are reported on $Cs_2Te_4{}^{IV}O_9$. The XRD Rietveld refinement for this compound was in perfect agreement with the structure previously determined by Loopstra and Goubitz,[15] and for this reason, it has been selected as the standard tellurite for the XAS experiments.

The absorption edges, defined as the inflection points of the absorption spectra (hence obtained as the zero of the second derivative), are summarized in Table 4.

In general, a clear shift of the absorption edge is observed with increasing oxidation state of the element. For the Mo K-edge, Cs_2MoO_4 and the $Cs_2Mo_{1-x}Te_xO_4$ solid solutions have absorption edges around 20015 eV, clearly higher than metallic Mo (20000 eV) and $Mo^{IV}O_2$ (20012 eV), and in line with the $Mo^{VI}O_3$ standard (20016 eV). Moreover, similarly to $Mo^{VI}O_3$ (but even more evident), all the $Cs_2Mo_{1-x}Te_xO_4$ samples present a marked pre-edge feature (for these spectra presenting a pre-edge, the E_0 has been taken on the second, main edge). This is characteristic of short, highly covalent Mo−O bonds in tetrahedral geometry, which enhance 4d-5p mixing in Mo through their hybridization with O(2p).[29−32] It can be confirmed that molybdenum is hexavalent and in tetrahedral MoO_4 units in all the $Cs_2Mo_{1-x}Te_xO_4$ solid solutions. Indeed, the pre-edge intensity is even more marked in the solid solutions than in MoO_3, suggesting a stronger covalency and shorter Mo−O bonds. In fact, the transition is dipole forbidden for a regular octahedra but appears in MoO_3 as a shoulder due to the distortion of the MoO_6 octahedra in that compound. Its intensity is related to the degree of octahedral distortion.

For the Te K-edge, there was no Te^{VI} standard available. However, because of the electroneutrality, tellurium is expected to be in the oxidation state +VI in the investigated materials. In support of this hypothesis, both $Cs_2Mo_{0.5}Te_{0.5}O_4$ and $Cs_2Mo_{0.2}Te_{0.8}O_4$ have an absorption energy equal (within the uncertainty limit) to that of pure Cs_2TeO_4 (31821 eV) and the values are more than 1 eV higher than those of $Te^{IV}O_2$ and

https://dx.doi.org/10.1021/acs.inorgchem.0c01307
Inorg. Chem. 2020, 59, 10172−10184

Table 3. Refined Atomic Positions in Cs_2TeO_4 and $Cs_2Mo_{0.5}Te_{0.5}O_4$[a,b]

atom	ox. state	Wyckoff	x	y	z	occ.	B_{eq} (Å^2)
				Cs_2TeO_4			
Cs1	+1	4c	0.4145(9)	0.25	0.6714(8)	1	3.3(2)
Cs2	+1	4c	−0.2849(7)	0.25	−0.0055(9)	1	2.9(3)
Te	+6	4c	0.4200(9)	0.25	0.2213(7)	1	2.3(2)
O1	−2	4c	0.425(2)	0.25	0.0109(7)	1	5.7(3)
O2	−2	4c	0.5639(8)	0.25	0.302(1)	1	3.7(3)
O3	−2	8d	0.3475(7)	0.0289(9)	0.2921(9)	1	4.7(2)
				$Cs_2Te_{0.5}Mo_{0.5}O_4$			
Cs1	+1	4c	0.4162(9)	0.25	0.6713(7)	1	3.0(2)
Cs2	+1	4c	−0.2887(6)	0.25	−0.0098(9)	1	2.4(2)
Te	+6	4c	0.4208(8)	0.25	0.2231(6)	0.5	2.0(2)
Mo	+6	4c	0.4208(8)	0.25	0.2231(6)	0.5	2.0(2)
O1	−2	4c	0.424(1)	0.25	0.0170(6)	1	4.9(3)
O2	−2	4c	0.5665(8)	0.25	0.300(1)	1	3.8(3)
O3	−2	8d	0.3501(6)	0.0284(9)	0.2945(8)	1	4.1(2)

[a] *Pcmn* setting of the space group n.°62. [b] Anisotropic atomic displacement factors are reported in the Supporting Information.

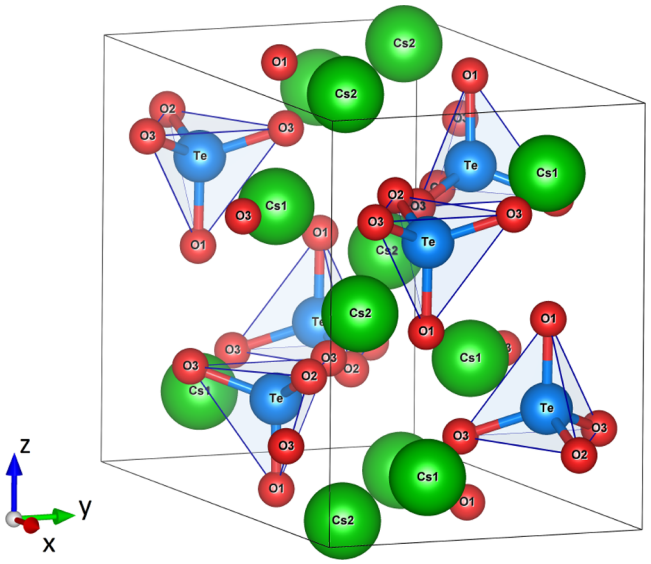

Figure 3. Sketch of the Cs_2TeO_4 crystal structure. Cs atoms are represented in green, Te/Mo in blue, and oxygen atoms in red.

$Cs_2Te_4^{IV}O_9$. We believe that the present measurements can serve as reference standards for future studies on tellurium-containing materials.

3.4. Local Structure Studies by EXAFS. The experimental EXAFS data and the relative Fourier transform (FT) collected at the Mo K-edge on Cs_2MoO_4 and $Cs_2Mo_{1-x}Te_xO_4$, with x = 0.05, 0.10, 0.50, and 0.80, are shown in Figure 5 (open symbols). All the data show a very similar shape. The FT of the data exhibit a first, very intense peak at $R + \Delta R \cong 1.4$ Å, as well as a low intensity peak around 3.6 Å (see also Figure 6).

The crystallographic structure obtained from neutron diffraction (Figure 3) was used as the input to fit the EXAFS data. The Mo (or Te) atom is in the center of a tetrahedron. According to the neutron diffraction refinement, this tetrahedron is not regular and three slightly different Mo−O distances are present. For example, for pure Cs_2MoO_4, Mo−O_1 = 1.76 Å, Mo−O_2 = 1.80 Å, and Mo−O_3 = 1.77 Å, the latter with a multiplicity equal to 2. These three neighboring shells are very close and difficult to differentiate by EXAFS. Indeed, the distance resolution ΔR is equal to $\pi/2\Delta k$, where Δk is the range of the data in the k-space. In our case, for the data collected at the Mo K-edge, ΔR = 0.11 Å. Therefore, it is not possible to differentiate the three Mo−O distances and the EXAFS data were fitted using one single oxygen coordination shell, formed of four atoms. Besides the four oxygen in tetrahedral coordination, the next Mo neighbor is a Cs atom, at a distance of 3.78 Å (for Cs_2MoO_4), followed by a neighbor shell composed of three Cs atoms at a distance ∼3.89 Å. Again, these two distances are hardly distinguishable by EXAFS, because of the weak amplitude of these contributions. This is particularly true for these further shells, since the contribution to EXAFS is rapidly dumped with increasing distance. For this reason, the four Cs atoms were included in a single shell for the fit. Finally, a multiple O−Mo−O diffusion path, within the MoO_4 tetrahedron and corresponding to an additional distance around 3.5 Å, was also included in the EXAFS model. For the latter, no supplementary fit parameters were introduced since the number of atoms, the distance, and the σ^2 factor were related to the values used in the Mo−O single scattering path. The inclusion of this multiple scattering path is essential because it creates destructive interference with the Mo−Cs path in the EXAFS spectrum. This interference is one of the reasons of the low intensity of the second peak (around 3.6 Å), together with the high values of the Mo−Cs distance and the Debye−Waller factor of this path (see Table S1 in the Supporting Information). More details on the interference between the paths are also provided in the Supporting Information. The contribution of the three paths to the EXAFS fit is shown in Figure 6 for Cs_2MoO_4 (similar results are obtained for the other compositions).

A generally good agreement between the fits and the experimental data was obtained for all the compositions, as shown in Figure 5 (experimental data shown with open symbols, fits shown with solid lines). The fitted coordination number and the σ^2 factors for the two neighboring shells, which are provided in the Supporting Information Table S1, are consistent with the adopted structural model. The obtained Mo−O and Mo−Cs bond distances, for each composition, are reported in Table 5 and are compared to the average distances obtained from neutron diffraction (for x = 0.05, 0.10, and 0.80, the distances were estimated by interpolation). The EXAFS Mo−O distance, equal to 1.78(Å), is shorter than the average

https://dx.doi.org/10.1021/acs.inorgchem.0c01307
Inorg. Chem. 2020, 59, 10172−10184

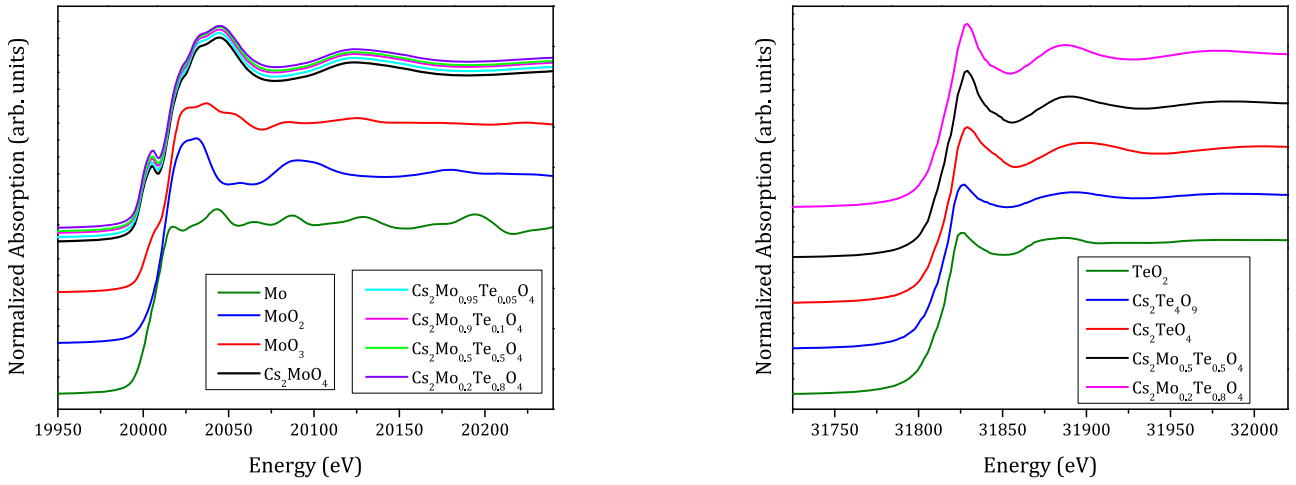

(a) Mo K-edge (b) Te K-edge

Figure 4. XANES spectra at the (a) Mo K-edge and (b) Te K-edge.

Table 4. Absorption Edges, Defined as the Zero Crossing of the Second Derivative[a]

	E_0 (eV)	
sample	Mo−K	Te−K
$Cs_2Mo_{0.95}Te_{0.05}O_4$	20015	–
$Cs_2Mo_{0.90}Te_{0.10}O_4$	20015	–
$Cs_2Mo_{0.50}Te_{0.50}O_4$	20015	31821
$Cs_2Mo_{0.20}Te_{0.80}O_4$	20015	31821
Cs_2MoO_4	20015	–
Cs_2TeO_4	–	31821
Mo^0	20000	–
$Mo^{4+}O_2$	20012	–
$Mo^{6+}O_3$	20016	–
$Te^{4+}O_2$	–	31819
$Cs_2Te_4{}^{+4}O_9$	–	31819

[a]Data are provided with an uncertainty of 1 eV.

Mo−O bond length in MoO_3, equal to 1.86(1) Å,[33,34] confirming the previous hypothesis based on the pre-edge intensity of the XANES.

The interatomic distances obtained from ND and EXAFS are generally in good agreement, within the experimental uncertainties. However, while the Mo−Cs distances obtained by EXAFS increase with the Te content, in accordance with the neutron data, the EXAFS Mo−O distance is constant throughout all the compositions. According to the neutron diffraction data, a small but detectable increase of the M−O ($M = Mo_{1-x}Te_x$) distance should also be observed, i.e., a difference of ∼0.03 Å between Cs_2MoO_4 and $Cs_2Mo_{0.20}Te_{0.80}O_4$. However, while the neutron diffraction data provide averaged data for the shared site between Te and Mo, the EXAFS gives information specific to the local environment around Mo. The XRD and neutron diffraction data reveal an expansion of the unit cell with the Te addition (consistent with the increase of the Mo−Cs distance), but the

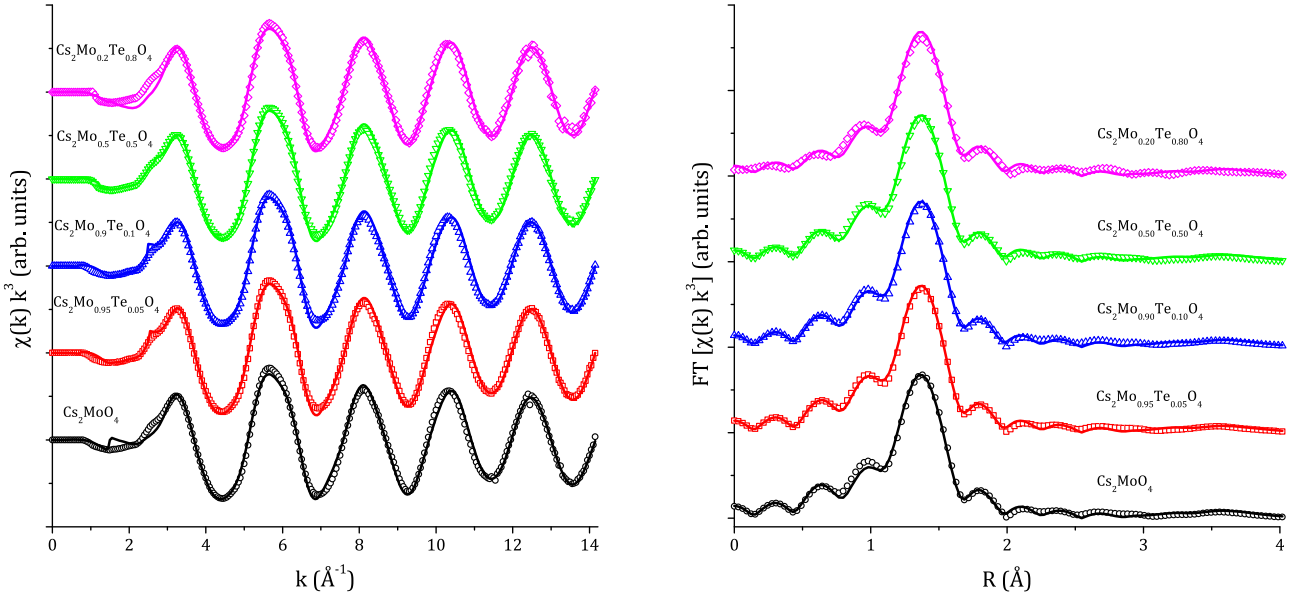

Figure 5. EXAFS data ($\chi(k)k^3$) and their Fourier transforms at the Mo K-edge. FT boundaries: 3.5−14 $Å^{-1}$, dk = 2 $Å^{-1}$.

https://dx.doi.org/10.1021/acs.inorgchem.0c01307
Inorg. Chem. 2020, 59, 10172−10184

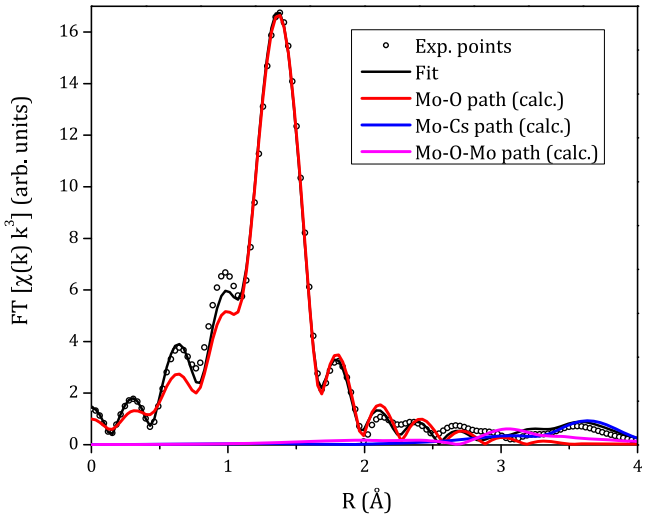

Figure 6. EXAFS Fourier transform of the Mo K-edge of Cs_2MoO_4. FT boundaries: 3.5−14 $Å^{-1}$, dk = 2 $Å^{-1}$.

Table 5. Comparison of the Mo−O and Mo−Cs Distances Obtained from EXAFS and Neutron Diffraction[b]

	Mo−O distance (Å)		Mo−Cs distance (Å)	
sample	neutron	EXAFS	neutron	EXAFS
Cs_2MoO_4	1.770(2)	1.78(1)	3.880(2)	3.89(2)
$Cs_2Mo_{0.95}Te_{0.05}O_4$	1.776[a]	1.78(1)	3.880[a]	3.90(2)
$Cs_2Mo_{0.90}Te_{0.10}O_4$	1.778[a]	1.78(1)	3.883[a]	3.90(2)
$Cs_2Mo_{0.50}Te_{0.50}O_4$	1.785(1)	1.78(1)	3.913(1)	3.91(2)
$Cs_2Mo_{0.20}Te_{0.80}O_4$	1.799[a]	1.78(1)	3.924[a]	3.91(2)

[a]Neutron data are available only for x(Te) = 0, 0.50, and 1; for the other compositions, the distances were obtained by interpolation. [b]The reported Mo−O distances from neutron diffraction correspond to the average of the four Mo−O tetrahedral distances.

EXAFS data show that the localized, strongly covalent Mo−O bond is unaffected by the tellurium presence. The Mo−O distance is the same in all the solid solutions, despite the large range of compositions investigated. This means that the Te−O distance must be responsible for the variation in the average distances obtained by neutron diffraction in the shared Te/Mo tetrahedra. The Te K-edge (>31 keV) is at the limit of the energy range that can be probed at the BM26A beamline, with the configuration adopted for the experiment. Hence, only the Te XANES data are exploited in this work.

3.5. Thermal Expansion and Phase Transition in Cs_2TeO_4. With Cs_2TeO_4 being isostructural with Cs_2MoO_4 at room temperature, the existence of a phase transition from the *Pcmn* orthorhombic structure (α form noted o-Cs_2TeO_4) to a hexagonal phase (β form noted h-Cs_2TeO_4) at high temperature is to be expected by analogy with the results on Cs_2MoO_4.[20] To confirm this hypothesis, high-temperature X-ray diffraction measurements were performed in this work on Cs_2TeO_4, from 298 to 1073 K (Figure 7) in dry air.

A sudden disappearance of some of the weak diffraction peaks was observed on heating, confirming a change in crystal structure between 713 and 723 K (Figure 7). As already discussed, below the transition point, the o-Cs_2TeO_4 structure corresponds to the room-temperature orthorhombic *Pcmn* model reported by Weller et al.,[35] an isotype of Cs_2SO_4,[36] Cs_2CrO_4[37] and Cs_2MoO_4.[38] Beyond 723 K, the structure becomes hexagonal (h-Cs_2TeO_4), following the usual transition scheme of this family of compounds. The systematic *hhl*, $l = 2n$ existence rule accounts for the $P6_3mc$ (or $P6_3/mmc$) space group commonly observed for the high temperature forms of the isotypes, instead of the $P\bar{3}m1$ symmetry proposed by Cordfunke et al.[39] The XRD Rietveld refinement of the XRD data at 773 K is shown in Figure 8, and the results are reported in Table 6. First refined in the $P6_3mc$ polar group from the 773 K data, the crystal structure of the h-form proved

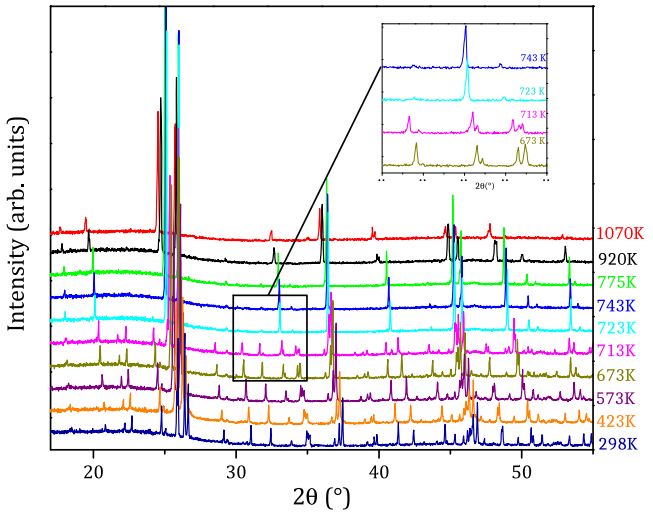

Figure 7. Thermal evolution of the XRD patterns of Cs_2TeO_4 between 298 and 1073 K, evidencing the phase transition.

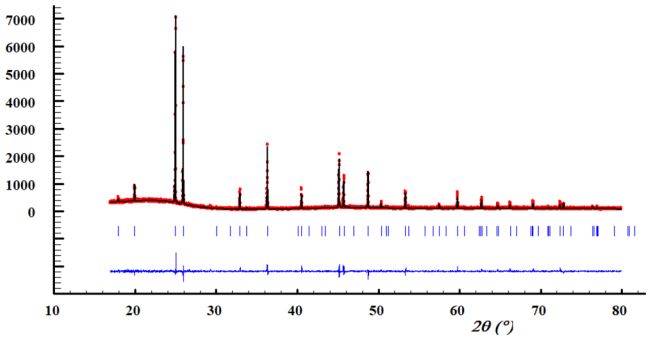

Figure 8. Rietveld plot for h-Cs_2TeO_4 at 773 K. Comparison between the observed Y_{obs} (in red) and calculated Y_{calc} (in black) X-ray diffraction patterns. $Y_{obs} - Y_{calc}$ (in blue) is the difference between the experimental and calculated intensities. The Bragg reflections' angular positions are also marked. Measurement at λ = Cu − Kα1.

Table 6. Refined Atomic Positions in h-Cs_2TeO_4 Derived from the X-ray Diffraction Refinement at 773 K[b]

atom	Wyckoff	x	y	z	occ.	B_{iso}* (Å²)
Cs1	2a	0	0	0	1	8.3(3)
Cs2	2d	1/3	2/3	3/4	1	11.6(6)
Te	2c	1/3	2/3	1/4	1	4.8(4)
O1	12k	0.189(3)	2x	0.317(5)	1/2	20(1)
O2	12k	0.24(1)	2x	0.08(1)	1/6	20(1)

[a]B_{eq}* (Å²) for cations: Cs1: B_{11} = 8.6(4), B_{33} = 7.7(5), B_{12} = 4.3(4). Cs2: B_{11} = 6.0(5), B_{33} = 22.7(6), B_{12} = 3.0(5). Te: B_{11} = 3.2(3), B_{33} = 7.8(4), B_{12} = 1.6(3). [b]Space group $P6_3/mmc$: a = 6.8661(8) Å, c = 8.897(1) Å. Bond lengths: Te−O1 = 1.81(2) Å; Te−O2 = 1.83(1) Å; 2.79 < Cs1−O < 3.58 Å; 3.16 < Cs2−O < 3.84 Å.

https://dx.doi.org/10.1021/acs.inorgchem.0c01307
Inorg. Chem. 2020, 59, 10172−10184

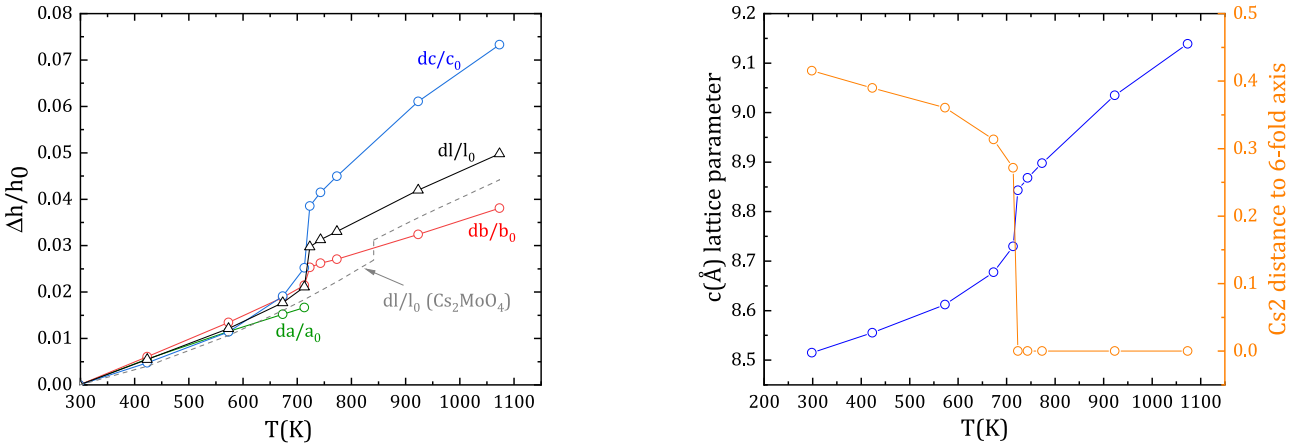

Figure 9. (a) Relative linear thermal expansion of Cs_2TeO_4 along the crystallographic axes. (b) Thermal variation of the *c*-parameter (left scale) and the distance of the Cs2 atoms to its position in the high temperature form (right scale). Error bars are smaller than the size of the dots.

consistent with the $P6_3/mmc$ supergroup owing to the location of the cations very close to the special positions at z = 0, 1/4, and 3/4, as well as the [0 0 ±1] disorder of the TeO_4 tetrahedron. The same symmetry was observed in *h*-Cs_2MoO_4,[20] but in the tellurate, the apical O2 atom seems to split onto three sites around the axial position (see the Fourier map in the Supporting Information Figure S3) instead of six in the molybdate. Conceivably, the whole TeO_4 tetrahedron undergoes this double (upside-down and tilt) disorder; hence, the very high values of the atomic displacement parameter of the oxygen atoms.

The relative linear thermal expansion plots $((h - h_0)/h_0) = \Delta h/h_0 = f(T)$, where $h = (a, b, c, l)$, $h_0 = (a_0, b_0, c_0, l_0)$, and $l_0 = (a_0b_0c_0)^{1/3}$ are the reference lengths at room temperature (Figure 9a), are very similar to those reported for Cs_2MoO_4,[20] showing anisotropic thermal expansion behavior. Here also the phase transition goes together with a pronounced break in the cell volume and the *c*-parameter (both +1.3%), while the cell surface in the (001) plane evolves continuously. Indeed, the transition corresponds to the sudden alignment of the Cs2 atoms along the 6-fold axis, but the phenomenon is preceded by a continuous shift, which accelerates between 573 and 623 K, as shown in Figure 9b, resulting in the increased slope of the *c* linear expansion. As established previously for Cs_2MoO_4,[20] both the high global expansion, high atomic displacement factors, and orientation disorder of the TeO_4 tetrahedron result from the very weak Cs−O bonds.

The relative linear thermal expansion follows a polynomial evolution as a function of temperature $T(K)$:

- in the orthorhombic domain:

$$dl/l_0 = -(6.8 \pm 3.6) \times 10^{-3} + (1.2 \pm 1.0) \times 10^{-5}T + (3.7 \pm 1.5) \times 10^{-8}T^2 \quad (3)$$

- in the hexagonal domain:

$$dl/l_0 = (-1.011 \pm 0.001) \times 10^{-2} + (5.7 \pm 0.1) \times 10^{-5}T \quad (4)$$

It is worth noting that the relative linear thermal expansion of Cs_2TeO_4 is even higher than that of Cs_2MoO_4, up to 29% at the maximum temperature reached (1073 K).

3.6. Transition Temperatures and Transition Enthalpy Determinations. The existence of a phase transition in Cs_2TeO_4, as evidenced from the X-ray diffraction experiments, was moreover confirmed by differential scanning calorimetry. A clear thermal event was detected in the heat flow curve at $T_{tr}(Cs_2TeO_4)$ = (712 ± 5) K, before the congruent melting event observed at $T_{fus}(Cs_2TeO_4)$ = (1187 ± 5) K (Figure 10).

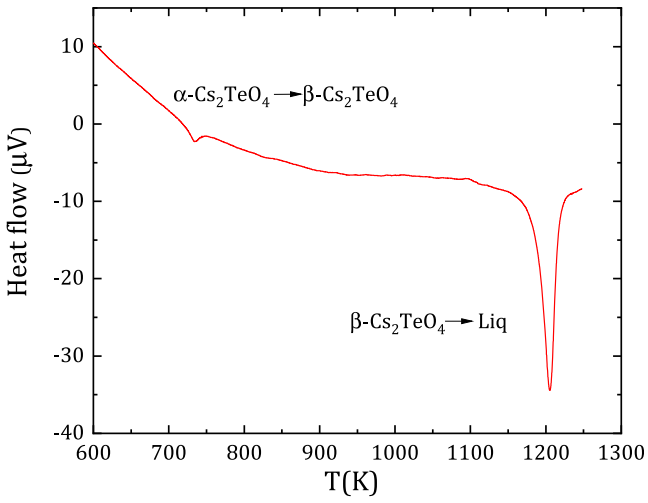

Figure 10. Heat flow signal versus temperature collected for Cs_2TeO_4.

The measured solid solution compositions also showed a similar phase transition, with a transition temperature decreasing progressively when increasing the Te/(Te + Mo) content (see Table 8 and Figures 12 and 13).

The transition enthalpies of the α to β phase transition in $Cs_2Mo_{1-x}Te_xO_4$ solid solutions (x = 0, 0.2, 0.5, 1) (from the orthorhombic to the hexagonal structure) were furthermore determined in this work by measuring the solid solution compositions together with a reference material of well-known transition enthalpy. This configuration allows us to derive for each individual measurement cycle the detector sensitivity,

https://dx.doi.org/10.1021/acs.inorgchem.0c01307
Inorg. Chem. 2020, 59, 10172−10184

Table 7. Transition Enthalpy Data Collected by DSC at Atmospheric Pressure[a]

m(sample) (mg)	m(ref) (mg)	$\Delta_{tr}H_m°$(ref) (kJ mol^{-1})	A_{ref} (μV s)	s_{ref} (μV mW^{-1})	A_{sample} (μV s)	$\Delta_{tr}H_m°$(sample) (kJ mol^{-1})
			Cs_2MoO_4 versus Al reference			
78.24	19.0	10.711	2980.62	0.3952	422.59	5.06
89.17	19.0	10.711	3105.49	0.4117	448.89	4.53
93.82	19.0	10.711	3004.55	0.3983	424.89	4.21
average						**(4.60 ± 0.43)**
			$Cs_2Mo_{0.8}Te_{0.2}O_4$ versus Al reference			
93.06	18.9	10.711	2093.46	0.3209	272.80	3.95
120.39	18.9	10.711	2300.50	0.3526	364.51	3.71
96.46	18.9	10.711	2173.24	0.3331	249.02	3.35
average						**(3.83 ± 0.17)**
			$Cs_2Mo_{0.5}Te_{0.5}O_4$ versus Al reference			
71.84	19.0	10.711	2984.98	0.4551	217.47	2.94
114.74	19.0	10.711	3002.77	0.4578	354.79	2.98
85.16	19.0	10.711	3005.72	0.4583	255.59	2.89
average						**(2.94 ± 0.05)**
			$Cs_2Mo_{0.5}Te_{0.5}O_4$ versus Na_2MoO_4 reference			
94.5	47.4	22.61	3157.26	0.6073	335.52	2.58
147.63	47.8	22.61	3179.2	0.6056	608.00	3.00
average						**(2.79 ± 0.30)**
			Cs_2TeO_4 versus Al reference			
90.65	12.2	10.711	1934.57	0.4594	243.40	2.67
92.89	12.2	10.711	1958.93	0.4651	239.35	2.53
97.17	12.2	10.711	1887.68	0.4482	267.19	2.81
average						**(2.67 ± 0.14)**

[a]The quoted uncertainties correspond to the standard deviations.

which is assumed to remain the same at the temperatures of the transition events of the sample and reference. Typical curves of the record heat flow signal are shown in Figures S4 and S5. Note that the opposite directions for the sample and reference (endothermic) events are due to the different positioning in the reference and sample crucibles, respectively.

Aluminum was chosen as the reference material, since it shows a melting temperature close to the sample transition event without overlapping, and it has a well-known melting enthalpy equal to 10.711 kJ mol^{-1} at T_{fus} = 933.5 K.[40] It appeared, however, that a correction factor had to be applied to the sensitivity factor to match the reported enthalpy of transition of Cs_2MoO_4 as recommended in the review of Cordfunke and Konings,[41] i.e., (4.6 ± 0.1) kJ mol^{-1}.[41] The necessity for this correction factor is believed to be related to the very different thermal properties (heat capacity and thermal conductivity) of the oxide and metallic materials. The same correction factor was applied to the other compositions (x = 0.2, 0.5, 1). The reliability of the method was moreover checked by measuring the transition enthalpy of $Cs_2Mo_{0.5}Te_{0.5}O_4$ against an oxide reference material, namely, Na_2MoO_4. The transition enthalpy was calculated against the α to β phase transition in Na_2MoO_4 (from a cubic $Fd\bar{3}m$ to an orthorhombic structure [Note: Bottelberghs and van Buren[42] suggested $Pbn2_1$ as the most probable space group, but a complete structure determination is lacking.]), whose transition enthalpy is equal to (22.61 ± 0.5 kJ mol^{-1}) as reported by Sugawara et al.[43] In this case, the sample and reference materials should have comparable thermal properties, and no correction factor was applied. The derived transition enthalpy for $Cs_2Mo_{0.5}Te_{0.5}O_4$ using the Na_2MoO_4 reference was found equal to (2.79 ± 0.30) kJ mol^{-1}, in very good agreement within the uncertainty with the value derived with the Al reference, i.e., (2.94 ± 0.05) kJ mol^{-1}, which gives us good confidence in the accuracy of the data and reliability of the method. The individual and averaged values obtained for each composition are listed in Table 7 and shown in Figure 11. A progressive decrease in the transition enthalpy value is observed when the tellurium content increases. The transition enthalpy for the Cs_2TeO_4 end-member was found as (2.67 ± 0.14) kJ mol^{-1}.

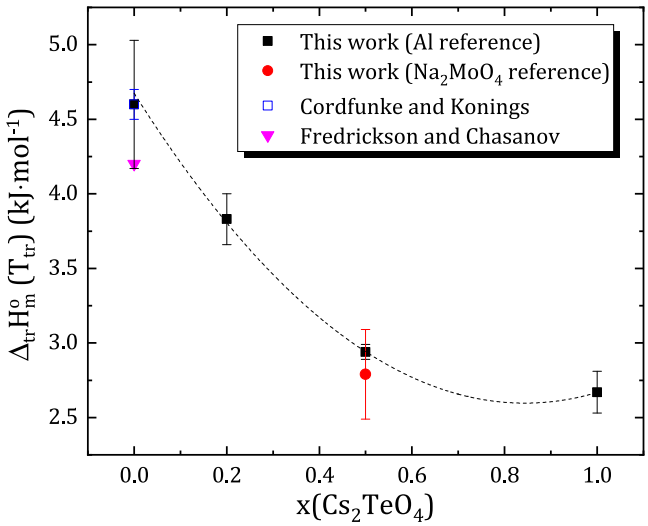

Figure 11. Evolution of the α to β transition enthalpy as a function of composition. The dotted line only serves as a guide for the eye.

3.7. Solidus and Liquidus Equilibria in the Cs_2MoO_4–Cs_2TeO_4 Phase Diagram. In addition to the phase transition temperatures in the $Cs_2Mo_{1-x}Te_xO_4$ solid solutions, the onset of the second thermal event was used to derive solidus temperatures (see Figures 12 and 14) in the Cs_2MoO_4–

https://dx.doi.org/10.1021/acs.inorgchem.0c01307
Inorg. Chem. 2020, 59, 10172−10184

Cs_2TeO_4 phase diagram. The phase equilibria points collected for all compositions are listed in Table 8. The liquidus could not be distinguished in the heat flow curves, however, due to the too high proximity with the solidus equilibria. The latter points were subsequently used to develop for the first time a thermodynamic model for the Cs_2MoO_4–Cs_2TeO_4 system using a regular solution model as detailed in the next section.

Table 8. Transition Temperatures Collected in the Cs_2MoO_4–Cs_2TeO_4 Phase Diagram by DSC[a]

composition	$T_{\alpha-\beta}$ (K)	T_{fus} (K)	$T_{solidus}$ (K)
Cs_2MoO_4	(839 ± 5)	(1226 ± 5)	
$Cs_2Mo_{0.9}Te_{0.1}O_4$	(826 ± 5)		(1215 ± 10)
$Cs_2Mo_{0.8}Te_{0.2}O_4$	(804 ± 5)		(1214 ± 10)
$Cs_2Mo_{0.6}Te_{0.4}O_4$	(785 ± 5)		(1198 ± 10)
$Cs_2Mo_{0.5}Te_{0.5}O_4$	(770 ± 5)		(1199 ± 10)
$Cs_2Mo_{0.4}Te_{0.6}O_4$	(760 ± 5)		(1196 ± 10)
$Cs_2Mo_{0.2}Te_{0.8}O_4$	(730 ± 5)		(1194 ± 10)
$Cs_2Mo_{0.1}Te_{0.9}O_4$	(726 ± 5)		(1182 ± 10)
Cs_2TeO_4	(712 ± 5)	(1187 ± 5)	

[a]See Figures 12, 13, and 14.

3.8. Regular Solution Model of the Cs_2MoO_4–Cs_2TeO_4 System. For a binary system such as Cs_2MoO_4–Cs_2TeO_4, where the solid and liquid solutions show similar physicochemical properties, one could expect an ideal or nearly ideal behavior. The solidus and liquidus lines in an ideal system, in which the heat capacities of the solid and liquid end-member phases are equal or very close to being near the melting temperatures, can be expressed as a simple analytical function of the melting temperatures and fusion enthalpies of the two end-members.[44] When taking into account the heat capacity difference between the solid and liquid phases, the width of the two-phase field between the solidus and liquidus curves varies slightly. When comparing the case of an ideal behavior (solidus and liquidus equilibria in dotted lines) in Figure 14 with the measured experimental solidus points, it is clear that the system does not behave ideally but rather shows a negative deviation from ideal behavior. This means that the phase equilibria can be well-represented only when taking the excess Gibbs energy of mixing into consideration.

A regular solution model[45,46] was used in this work to optimize the Cs_2MoO_4–Cs_2TeO_4 phase diagram based on the collected equilibria points. In the latter model, the entropy of mixing is assumed to be ideal and the excess Gibbs energy of mixing is given solely by an enthalpic term equal to

$$\Delta_{mix}^{exc} G_m^o = \Omega x_{Cs_2MoO_4} x_{Cs_2TeO_4} \quad (5)$$

where Ω corresponds to the regular solution constant (also called interaction coefficient) assumed to be independent of temperature, and $x_{Cs_2MoO_4}$ and $x_{Cs_2TeO_4}$ are the molar fractions of the Cs_2MoO_4 and Cs_2TeO_4 end-members, respectively.

Three interaction parameters were optimized in this work, i.e., two for the solid solutions α-$Cs_2Mo_{1-x}Te_xO_4$ and β-$Cs_2Mo_{1-x}Te_xO_4$ and one for the liquid solution:

$$\Delta_{mix}^{exc} G_m^o(\alpha)/\mathrm{J\ K^{-1}\ mol^{-1}} = 2300 x_{Cs_2MoO_4} x_{Cs_2TeO_4} \quad (6)$$

$$\Delta_{mix}^{exc} G_m^o(\beta)/\mathrm{J\ K^{-1}\ mol^{-1}} = 2000 x_{Cs_2MoO_4} x_{Cs_2TeO_4} \quad (7)$$

$$\Delta_{mix}^{exc} G_m^o(\mathrm{liquid})/\mathrm{J\ K^{-1}\ mol^{-1}} = 1000 x_{Cs_2MoO_4} x_{Cs_2TeO_4} \quad (8)$$

The optimization was done by a "trial-and-error method" using the FactSage software based on the measured enthalpies of transitions for Cs_2MoO_4 and Cs_2TeO_4 and the collected phase equilibrium data (onset temperatures for the phase transitions in the solid solution and solidus points).

The computed phase diagram is shown in Figures 12, 13, and 14. The agreement with the experimental data is good within the experimental uncertainties. Because very little is known on the thermodynamic properties of Cs_2TeO_4 (only the enthalpy of formation has been reported by Cordfunke et al.[47]), a number of assumptions had to be made for the expressions of the Gibbs energy of the Cs_2TeO_4 end-member. The selected thermodynamic data for the thermodynamic model are listed in detail in the Supporting Information Section 3, together with a justification for the choice of the thermodynamic functions for this end-member composition. The present model offers a first basis for thermodynamic equilibrium calculations in the Cs_2MoO_4–Cs_2TeO_4 system. Nevertheless, for a comprehensive assessment of the JOG system and JOG chemistry, a complete CALPHAD assessment of the Cs–Te–Mo–O system would be necessary, in

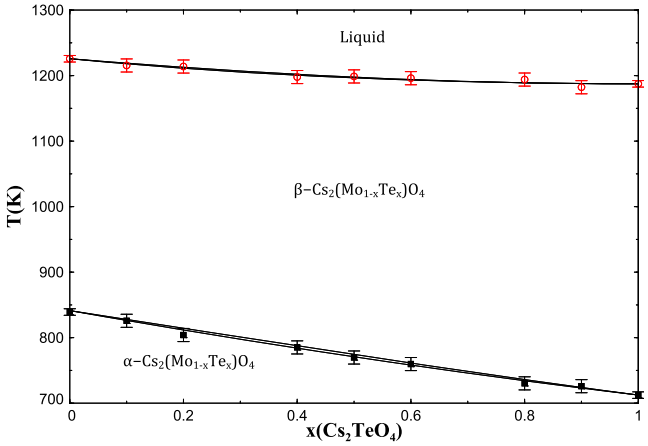

Figure 12. Phase equilibria points measured in this work (black squares and red circles) and regular solution model (solid lines) of the Cs_2MoO_4–Cs_2TeO_4 phase diagram.

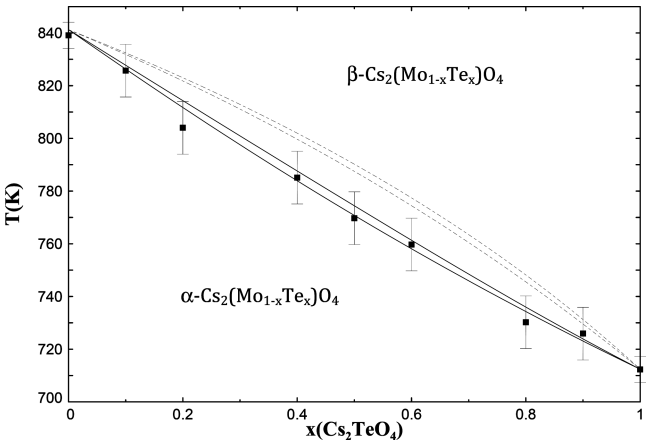

Figure 13. Phase equilibria points measured in this work and regular solution model of the Cs_2MoO_4–Cs_2TeO_4 phase diagram. Extended view of the phase transition equilibria (plain lines). The pseudo-binary phase diagram for an ideal behavior is also shown in dotted lines.

https://dx.doi.org/10.1021/acs.inorgchem.0c01307
Inorg. Chem. 2020, 59, 10172–10184

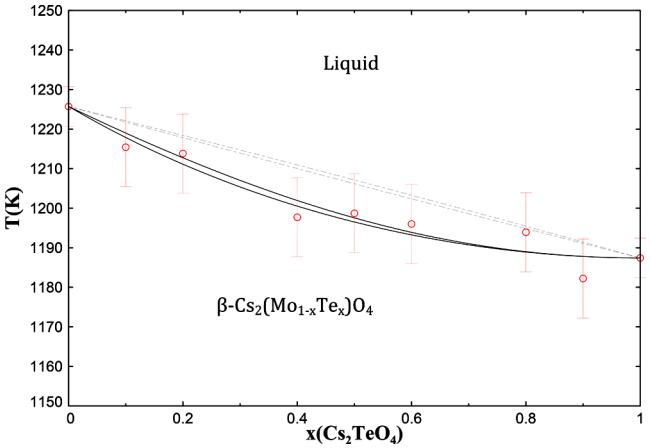

Figure 14. Phase equilibria points measured in this work and regular solution model of the Cs_2MoO_4–Cs_2TeO_4 phase diagram. Extended view of the solidus and liquidus curves (plain lines). The pseudobinary phase diagram for an ideal behavior is also shown in dotted lines.

particular to account for the effects of changes in oxygen potential with burn-up.

4. CONCLUSIONS AND IMPLICATIONS FOR THE SAFETY ASSESSMENT OF THE FUEL BEHAVIOR IN FNRS

In this work, new structural, thermodynamic, and phase diagram data on the Cs–Te–O and Cs–Mo–Te–O systems have been provided. In particular, this study focused on the Cs_2TeO_4 compound as it is, at room temperature, isostructural with Cs_2MoO_4, the major component of the JOG.

The existence of the $Cs_2Mo_{1-x}Te_xO_4$ solid solution over the complete composition range $0 < x < 1$ is reported for the first time. Combining room-temperature XRD, ND, and XAS, it has been shown that the solid solution obeys Vegard's law, i.e., a linear expansion of the lattice is observed by increasing the tellurium content. However, EXAFS data on the Mo K-edge have shown that the short, highly covalent Mo–O bonds are not influenced by the tellurium addition, and hence, the oxygen tetrahedral environment around Mo remains unchanged in the solid solution.

High-temperature XRD analysis was performed on Cs_2TeO_4 in order to obtain the coefficients of thermal expansion of this compound. These measurements highlighted also the presence of an $\alpha \rightarrow \beta$ phase transition at about 712 K, with a structural change from orthorhombic to hexagonal, equivalent to that exhibited by Cs_2MoO_4 at higher temperature (839 ± 5 K). This transition was also confirmed by DSC experiments, which were performed on various compositions of the $Cs_2Mo_{1-x}Te_xO_4$ solid solution. These measurements allowed us to determine the variation of the $\alpha \rightarrow \beta$ phase transition temperature with the tellurium content, as well as the enthalpy change associated with this transition. In addition, the congruent melting point of Cs_2TeO_4 and the *solidus* temperatures of the $Cs_2Mo_{1-x}Te_xO_4$ solid solutions were obtained. Thanks to these new phase diagram equilibria points, a first thermodynamic modeling assessment of the Cs_2MoO_4–Cs_2TeO_4 system is proposed.

The data reported in this work represent a step forward for the comprehension of the thermodynamic and thermal properties of the multi-element JOG system. Even if further studies are still necessary, some preliminary considerations can already be made on the Cs–Mo–Te–O sub-system, based on the results of this study. Typically, one of the major concerns in FNRs is the chemical interaction between the oxide pellet and the clading material, which can have an impact on the mechanical behavior of the fuel element. For that reason, it is important to evaluate the chemical and the mechanical interaction between the JOG and the clad (stainless steel). As shown in this work, the dissolution of tellurium in Cs_2MoO_4 causes a lattice expansion of this phase. This expansion could increase the mechanical stress sustained by the cladding and hence have deleterious effects on its integrity. However, it must be noticed that the available irradiation tests and associated post-irradiation examinations did not highlight failure of the cladding in the presence of the JOG;[2−8] on the contrary, some of the results seem to indicate a beneficial effect of the JOG formation on the fuel-clad mechanical interaction.[5] This could be due to a much higher visco-elasticity of the JOG phases compared to the fuel. Further investigations are needed on this point.

Thermal expansion properties are also essential to assess JOG-cladding and JOG-fuel interactions during the thermal cycles. The thermal expansion behavior of Cs_2MoO_4 was investigated by Wallez et al.[20] Concerns rise from the anisotropic thermal expansion of the high-temperature hexagonal phase, which can induce microcracks during the cycles, and from the difference between the thermal expansions of Cs_2MoO_4 and the fuel. The volume increase due to the $\alpha - \beta$ phase transition and the thermal expansion measured for pure Cs_2TeO_4 are very similar to those reported for Cs_2MoO_4, but shifted to lower temperatures. Therefore, the dilution of Te needs to be taken into account to assess the JOG-fuel interaction during thermal transients.

Finally, one of the most important properties for the safety of a nuclear reactor is the melting temperature of the fuel. As shown herein, the increase of Te content in the $Cs_2Mo_{1-x}Te_xO_4$ solid solution induces a regular decrease of the melting temperature, with a maximum difference of almost 130 K between the end-members. It is hence essential to take into account the possible dilution of tellurium into Cs_2MoO_4 under high oxygen potential conditions in order to determine the safety margin of operation of fast neutron reactors.

■ ASSOCIATED CONTENT

Supporting Information

The Supporting Information is available free of charge at https://pubs.acs.org/doi/10.1021/acs.inorgchem.0c01307.

Neutron diffraction pattern of $Cs_2Mo_{0.5}Te_{0.5}O_4$ and Rietveld refinement of the data; anisotropic atomic displacement factors data; EXAFS data fitted at the Mo K-edge; Fourier difference map of β-Cs_2TeO_4; heat flow curves for Cs_2TeO_4 and $Cs_2Mo_{0.5}Te_{0.5}O_4$; and details on the regular solution model of the Cs_2MoO_4–Cs_2TeO_4 system (PDF)

X-ray crystallographic files in CIF format (ZIP)

Accession Codes

CCDC 2000544–2000545 contain the supplementary crystallographic data for this paper. These data can be obtained free of charge via www.ccdc.cam.ac.uk/data_request/cif, or by emailing data_request@ccdc.cam.ac.uk, or by contacting The Cambridge Crystallographic Data Centre, 12 Union Road, Cambridge CB2 1EZ, UK; fax: +44 1223 336033.

https://dx.doi.org/10.1021/acs.inorgchem.0c01307
Inorg. Chem. 2020, 59, 10172−10184

AUTHOR INFORMATION

Corresponding Author

Anna L. Smith − *Delft University of Technology, Faculty of Applied Sciences, Radiation Science and Technology Department, 2629 JB Delft, The Netherlands;* orcid.org/0000-0002-0355-5859; Email: a.l.smith@tudelft.nl

Authors

Enrica Epifano − *Delft University of Technology, Faculty of Applied Sciences, Radiation Science and Technology Department, 2629 JB Delft, The Netherlands*

Andrea Volfi − *Politecnico di Milano, Department of Energy, Nuclear Engineering Division, 20156 Milano, Italy*

Maas Abbink − *Delft University of Technology, Faculty of Applied Sciences, Radiation Science and Technology Department, 2629 JB Delft, The Netherlands*

Hendrik Nieuwland − *Delft University of Technology, Faculty of Applied Sciences, Radiation Science and Technology Department, 2629 JB Delft, The Netherlands*

Lambert van Eijck − *Delft University of Technology, Faculty of Applied Sciences, Radiation Science and Technology Department, 2629 JB Delft, The Netherlands*

Gilles Wallez − *Chimie ParisTech, PSL University, CNRS, Institut de Recherche de Chimie Paris, 75005 Paris, France; UFR 926, Sorbonne Université, 75005 Paris, France*

Dipanjan Banerjee − *Department of Chemistry, KU Leuven, 30001 Leuven, Belgium;* orcid.org/0000-0002-1933-8066

Philippe M. Martin − *CEA, DES, ISEC, DMRC, Université de Montpellier, 34090 Marcoule, France*

Complete contact information is available at: https://pubs.acs.org/10.1021/acs.inorgchem.0c01307

Notes

The authors declare no competing financial interest.

ACKNOWLEDGMENTS

This work has received funding from the Euratom research and training programme 2014−2018 through the INSPYRE (Investigations Supporting MOX Fuel Licensing in ESNII Prototype Reactors) project under grant agreement no. 754329. The authors are thankful to G. Kauric and S. Mastromarino for their participation to the experiments at the ESRF.

REFERENCES

(1) Buckthorpe, D. In *Structural Materials for Generation IV Nuclear Reactors*; Yvon, P., Ed.; Woodhead Publishing: 2017.

(2) Tourasse, M.; Boidron, M.; Pasquet, B. Fission product behaviour in phenix fuel pins at high burnup. *J. Nucl. Mater.* **1992**, *188*, 49−57.

(3) Maeda, K.; Tanaka, K.; Asaga, T.; Furuya, H. Distributions of volatile fission products in or near the fuel-cladding gap of the FBR MOX fuel pins irradiated to high burn-up. *J. Nucl. Mater.* **2005**, *344*, 274−280.

(4) Uwaba, T.; Ito, M.; Mizuno, T.; Katsuyama, K.; Makenas, B. J.; Wootan, D. W.; Carmack, J. Irradiation performance of fast reactor MOX fuel pins with ferritic/martensitic cladding irradiated to high burnups. *J. Nucl. Mater.* **2011**, *412*, 294−300.

(5) Teague, M.; Gorman, B.; King, J.; Porter, D.; Hayes, S. Microstructural characterization of high burn-up mixed oxide fast reactor fuel. *J. Nucl. Mater.* **2013**, *441*, 267−273.

(6) Parrish, R.; Winston, A.; Harp, J.; Aitkaliyeva, A. TEM characterization of high burnup fast-reactor MOX fuel. *J. Nucl. Mater.* **2019**, *527*, 151794.

(7) Samuelsson, K.; Dumas, J.-C.; Sundman, B.; Lamontagne, J.; Guéneau, C. Simulation of the chemical state of high burnup $(U,Pu)O_2$ fuel in fast reactors based on thermodynamic calculations. *J. Nucl. Mater.* **2020**, *532*, 151969.

(8) Cappia, F.; Miller, B. D.; Aguiar, J. A.; He, L.; Murray, D. J.; Frickey, B. J.; Stanek, J. D.; Harp, J. M. Electron microscopy characterization of fast reactor MOX Joint Oxyde-Gaine (JOG). *J. Nucl. Mater.* **2020**, *531*, 151964.

(9) Dumas, J.-C. Etude des conditions de formation du Joint-Oxyde-Gaine dans les combustibles oxydes mixtes des reacteurs à neutrons rapides, observations et proposition d'un modèle de comportement des produits de fission volatils. Ph.D. Thesis, Institut National Polytechnique de Grenoble: Grenoble, France, 1995.

(10) Konings, R. J. M.; Cordfunke, E. H. P. The thermochemical properties of cesium molybdate, Cs_2MoO_4, from 298.15 to 1500 K. *Thermochim. Acta* **1988**, *124*, 157−162.

(11) Thi, T. N. P. Caractérisation et modélisation du comportement thermodynamique du combustible RNR-Na sous irradiation. Ph.D. Thesis, Ecole Doctorale Physique et Sciences de la Matière (Aix-Marseille University), 2014.

(12) Hoekstra, H. R. The Cs_2MoO_4-MoO_3 system. *Inorg. Nucl. Chem. Lett.* **1973**, *9*, 1291−1301.

(13) Cordfunke, E. H. P.; Konings, R. J. M. Thermochemical data for reactor materials and fission products: The ECN database. *J. Phase Equilib.* **1993**, *14*, 457−464.

(14) Thermodynamics of AdVanced Fuels, International Database (TAF-ID); www.oecd-nea.org/science/taf-id/ (accessed 2020).

(15) Loopstra, B. O.; Goubitz, K. The structures of four caesium tellurates. *Acta Crystallogr., Sect. C: Cryst. Struct. Commun.* **1986**, *42*, 520−523.

(16) Siritanon, T.; Li, J.; Stalick, J. K.; Macaluso, R. T.; Sleight, A. W.; Subramanian, M. A. $CsTe_2O_{6-x}$: Novel Mixed-Valence Tellurium Oxides with Framework-Deficient Pyrochlore-Related Structure. *Inorg. Chem.* **2011**, *50*, 8494−8501.

(17) Weller, M. T.; Pack, M. J.; Binsted, N.; Dann, S. E. The structure of cesium tellurate (VI) by combined EXAFS and powder X-ray diffraction. *J. Alloys Compd.* **1999**, *282*, 76−78.

(18) Cordfunke, E. H. P.; Smit-Groen, V. M. A DSC study of the phase diagram of the system TeO_2-Cs_2TeO_3. *Thermochim. Acta* **1984**, *80*, 181−183.

(19) Cordfunke, E. H. P.; Ouweltjes, W.; Prins, G. Standard enthalpies of formation of tellurium compounds III. Cs_2TeO_3, $Cs_2Te_2O_5$, $Cs_2Te_4O_9$, and Cs_2TeO_4. *J. Chem. Thermodyn.* **1988**, *20*, 569−573.

(20) Wallez, G.; Raison, P. E.; Smith, A. L.; Clavier, N.; Dacheux, N. High-temperature behavior of dicesium molybdate Cs_2MoO_4: Implications for fast neutron reactors. *J. Solid State Chem.* **2014**, *215*, 225−230.

(21) Rodriguez-Carvajal, J. Recent advances in magnetic structure determination by neutron powder diffraction. *Phys. B* **1993**, *192*, 55−69.

(22) van Eijck, L.; Cussen, L. D.; Sykora, G. J.; Schooneveld, E. M.; Rhodes, N. J.; van Well, A. A.; Pappas, C. Design and performance of a novel neutron powder diffractometer: PEARL at TU Delft. *J. Appl. Crystallogr.* **2016**, *49*, 1398−1401.

(23) Borsboom, M.; Bras, W.; Cerjak, I.; Detollenaere, D.; Glastra Van Loon, D.; Goedtkindt, P.; Konijnenburg, M.; Lassing, P.; Levine, Y. K.; Munneke, B.; Oversluizen, M.; Van Tol, R.; Vlieg, E. The Dutch-Belgian beamline at the ESRF. *J. Synchrotron Radiat.* **1998**, *5*, 518−520.

(24) Ravel, B.; Newville, M. ATHENA, ARTEMIS, HEPHAESTUS: data analysis for X-ray absorption spectroscopy using IFEFFIT. *J. Synchrotron Radiat.* **2005**, *12*, 537−541.

(25) Höhne, G. W. H.; Cammenga, H. K.; Eysel, W.; Gmelin, E.; Hemminger, W. The temperature calibration of scanning calorimeters. *Thermochim. Acta* **1990**, *160*, 1−12.

(26) Della Gatta, G.; Richardson, M. J.; Sarge, S. M.; Stølen, S. Standards, calibration, and guidelines in microcalorimetry. Part 2.

Calibration standards for differential scanning calorimetry (IUPAC Technical Report). *Pure Appl. Chem.* **2006**, *78*, 1455−1476.
(27) Shannon, R. D. Revised Effective Ionic Radii and Systematic Studies of Interatomic Distances in Halides and Chalcogenides. *Acta Crystallogr., Sect. A: Cryst. Phys., Diffr., Theor. Gen. Crystallogr.* **1976**, *32*, 751−767.
(28) Smith, A. L.; Kauric, G.; van Eijck, L.; Goubitz, K.; Wallez, G.; Griveau, J.-C.; Colineau, E.; Clavier, N.; Konings, R. J. M. Structural and thermodynamic study of dicesium molybdate $Cs_2Mo_2O_7$: Implications for fast neutron reactors. *J. Solid State Chem.* **2017**, *253*, 89−102.
(29) Aritani, H.; Tanaka, T.; Funabiki, T.; Yoshida, S.; Kudo, M.; Hasegawa, S. Structure of Mo-Mg Binary Oxides in Oxidized/Reduced States Studied by X-ray Absorption Spectroscopy at the Mo K-Edge and Mg K-Edge. *J. Phys. Chem.* **1996**, *100*, 5440−5446.
(30) Rocca, F.; Kuzmin, A.; Mustarelli, P.; Tomasi, C.; Magistris, A. XANES and EXAFS at Mo K-edge in $(AgI)_{1-x}(Ag_2MoO_4)_x$ glasses and crystals. *Solid State Ionics* **1999**, *121*, 189−192.
(31) Kuzmin, A.; Purans, J. Dehydration of the molybdenum trioxide hydrates $MoO_3{\cdot}nH_2O$: in situ x-ray absorption spectroscopy study at the Mo K edge. *J. Phys.: Condens. Matter* **2000**, *12*, 1959−1970.
(32) Lima, F. A.; Bjornsson, R.; Weyhermüller, T.; Chandrasekaran, P.; Glatzel, P.; Neese, F.; DeBeer, S. High-resolution molybdenum K-edge X-ray absorption spectroscopy analyzed with time-dependent density functional theory. *Phys. Chem. Chem. Phys.* **2013**, *15*, 20911−20920.
(33) Andersson, G.; Magneli, A.; Sillén, L. G.; Rottenberg, M. On the crystal structure of molybdenum trioxide. *Acta Chem. Scand.* **1950**, *4*, 793−797.
(34) Sitepu, H. Texture and structural refinement using neutron diffraction data from molybdite (MoO_3) and calcite ($CaCO_3$) powders and a Ni-rich Ni50.7Ti49.30 alloy. *Powder Diffr.* **2009**, *24*, 315−326.
(35) Weller, M. T.; Pack, M. J.; Binsted, N.; Dann, S. E. The structure of cesium tellurate (VI) by combined EXAFS and powder X-ray diffraction. *J. Alloys Compd.* **1999**, *282*, 76−78.
(36) Ogg, A. The crystal structure of the isomorphous sulfates of potassium, ammonium, rubidium, and cesium. *Philos. Mag.* **1928**, *5*, 354−371.
(37) Miller, J. J. The crystal structure of cesium chromate Cs_2CrO_4. *Z. Kristallogr. Kristallgeom. Kristallphys. Kristallchem.* **1938**, *99*, 32−37.
(38) Gonschorek, W.; Hahn, T. Die Kristallstruktur des Caesiummolybdats, Cs_2MoO_4. *Z. Kristallogr. Kristallgeom. Kristallphys. Kristallchem.* **1973**, *138*, 167−176.
(39) Cordfunke, E.; Vlaanderen, P. The structure of cesium tellurate (VI) by combined EXAFS and powder X-ray diffraction. Netherlands Energy Research Foundation, ECN, The Netherlands: Private Communication, PDF no. 37-1341, 1986.
(40) Chase, M.; Ed, J. *NIST-JANAF Thermochemical Tables*, monograph 9, 4th ed.; American Chemical Society, American Institute of Physics, National Bureau of Standards: New York, 1998.
(41) Cordfunke, E. H. P.; Konings, R. J. M. *Thermochemical Data for Reactor Materials and Fission Products*; Elsevier Science Publishers B.V.: 1990.
(42) Bottelberghs, P.H.; van Buren, F.R. Phase Relations, Dopant Effects, Structure, and High Electrical Conductivity in the Na_2WO_4-Na_2MoO_4 System. *J. Solid State Chem.* **1975**, *13*, 182−191.
(43) Sugawara, T.; Jin, K. Enthalpy and heat capacity of Na_2MoO_4 and $CaMoO_4$. *Thermochim. Acta* **2018**, *669*, 185−193.
(44) Stølen, S.; Grande, T.; Allan, N. L. *Chemical Thermodynamics of Materials: Macroscopic and Microscopic Aspects*; John Wiley & Sons, Ltd: 2004.
(45) Hildebrand, J. H. Solubility. XII. Regular solutions. *J. Am. Chem. Soc.* **1929**, *51*, 66.
(46) Pelton, A.; Thompson, W. Phase Diagrams. *Prog. Solid State Chem.* **1975**, *10*, 119−155.
(47) Cordfunke, E. H. P.; Cluistra, R.; Van Miltenburg, J. C. The thermodynamic properties of six compounds in (tellurium+oxygen +hydrogen) from 10 to 1000 K. *J. Chem. Thermodyn.* **1985**, *17*, 1079−1089.

https://dx.doi.org/10.1021/acs.inorgchem.0c01307
Inorg. Chem. 2020, 59, 10172−10184